RSC Advances

PAPER

View Article Online
View Journal | View Issue

Cite this: *RSC Adv.*, 2024, **14**, 37546

Efficient photocatalytic performance of hydrogen bonding between P25 and microcrystalline cellulose aerogel†

Junhao Zen,[a] Di Zhang,[a] Guoliang Dou,[a] Qingming Zeng*[a] and Jian Zhang *[ab]

Received 2nd October 2024
Accepted 7th November 2024

DOI: 10.1039/d4ra07087a

rsc.li/rsc-advances

A series of MC/P25 composite aerogels (MCAPs) were newly designed by the sol–gel method and CO_2 supercritical drying technology. Under visible light irradiation, the optimized MCAP exhibits enhanced photocatalytic performance with a AO7 degradation rate of 0.01746 min^{-1}, which is 6.6 times higher than that of P25. The enhanced photocatalytic performance can be mainly ascribed to the constructed H-bonds between microcrystalline cellulose and P25. Photocurrent–time curves and photoluminescence spectra all certified the increased photogenerated carrier transfer rates of MCAP due to the presence of H-bonds. This work indicates that the presence of H-bonds can efficiently transfer photo-induced electrons and limit the recombination of photogenerated carriers. Furthermore, as a 3D aerogel photocatalyst, the photocatalytic stability is improved.

1. Introduction

Overuse of toxic dyes in various industries has caused serious environmental problems. Many novel photocatalysts have been designed to photoreduce toxic dyes, such as zinc indium sulfide-nanostructured photocatalysts, three-dimensional zinc oxide nanostructures, AgCl nanoparticle-decorated $ZnWO_4$ nanorods, SiO_2/BiOCl composites, and so on.[1–4] In recent years, organic–inorganic composites have attracted a lot of attention due to their excellent structure adaptability.[5] Among them, cellulose-modified semiconductors for photocatalysis research are a typical example.[6,7] Although cellulose itself has no direct photocatalytic activity, it can promote the performance of semiconductor photocatalysts in two ways, namely, as an auxiliary or a biological template.[8] When cellulose is used as an auxiliary agent, its good hydrophilicity may promote the reaction in the aqueous phase.[9] In addition, with its interleaved microfibers and rich surface functional groups, cellulose can also be used as a carrier to fix, disperse and even change the morphology of the semiconductor, thus improving its photocatalytic performance.[10] In particular, some cellulose porous materials are often used as auxiliary agents for photocatalysts,[11,12] and the composite catalysts will not only transform cellulose into the backbone substrate, so as to promote the transfer of photogenerated carriers, but also show large specific surface area, so as to provide more effective active sites. In addition, cellulose can be easily processed into a variety of block materials with high mechanical strength and flexibility, which is also conducive to the recovery of photocatalysts.[13,14]

For individual semiconductor catalysts, one serious problem limiting their photocatalytic performance is the recombination of their photogenerated carriers. Organic–inorganic composites can modulate the charge distribution and promote the migration of photogenerated carriers.[15] However, the simple physical mixing of organic and inorganic materials is little help in improving their photocatalytic performance. How to regulate the interface construction of organic and inorganic materials is the key problem. Effective interface construction can improve the migration rate of photogenerated carriers significantly. Yu *et al.*[16] designed carbonized glutaraldehyde (C-GA)/graphitic carbon nitride (CN) composite catalysts, where C-GA and CN were coupled by H-bonds, which showed enhanced photocatalytic performance by accelerating the charge transfer rate.[16] Wang *et al.*[17] also prepared a MC/g-C_3N_4 photocatalyst, which is connected by H-bonds and shows efficient photocatalytic performance.[17] These works all certified the efficient performance of H-bonds for photocatalysts.

Inspired by these works, designing organic–inorganic composite photocatalysts *via* constructing H-bonds is an innovative approach. P25 is a typical representative of an inorganic photocatalyst, which has good photocatalytic performance under ultraviolet light.[18] Many TiO_2 composite photocatalysts exhibit good photocatalytic performance.[19–22] MC is rich in hydroxyl groups and can be effectively combined with P25 through H-bonds, which can be used as an experimental model to verify the role of H-bonds in photocatalysis. In addition, MC can be prepared in the form of an aerogel, and many aerogel

[a]*Shandong Engineering Research Center for High Performance Silicone Rubber, Weifang 261000, P. R. China. E-mail: sduchemzhang@163.com*

[b]*Department of Chemistry and Chemical Engineering, Jining University, Qufu 273100, P. R. China*

† Electronic supplementary information (ESI) available. See DOI: https://doi.org/10.1039/d4ra07087a

composite photocatalysts have been widely studied and exhibit the advantages of high specific surface area, low cost, photostability, *etc.*[23–25] The combination of P25 and MC through H-bonds can ensure the stability of the P25 particles on the MC aerogel. Based on this, a MC/P25 composite aerogel was designed by the sol–gel method and CO_2 supercritical drying technology. By comparing the photocatalytic performance of P25 and the composite catalyst, it is shown that hydroxyl-rich materials can make up for the defects of traditional inorganic semiconductors to a certain extent and achieve enhanced photocatalytic performance.

2. Experimental

2.1 Materials

Microcrystalline cellulose (MC), NaOH and urea were purchased from Alfa-Aesar, P25 was purchased from Shanghai Deco Industrial Co., Ltd. Deionized water (DI) was made in the laboratory. All the reagents were used without further purification.

2.2 Synthesis of MC/P25 composite aerogels (MCAPs)

At room temperature, 0.6 g of NaOH was added into 8.1 g of H_2O in a beaker, and then 1.2 g of urea was added to the solution. After the dissolution of urea, 0.526 g of MC was added into the solution for 30 min with stirring. Then, the beaker was placed into a refrigerator at −20 °C. After 40 min, the beaker was taken out from the refrigerator, and the solution was stirred at room temperature for 20 min. A transparent solution was obtained. Then, 0.01052 g of P25 was added into the solution under stirring, and the solution was poured into a Petri dish, which was sealed and set in a water bath pot at 75 °C for 4 h. Then, the gel was formed. The gel was dipped in ethanol for 3 days, and the ethanol was replaced every 24 h. After that, the gel was dried by CO_2 supercritical drying technology at 8 MPa and 40 °C. The obtained sample was marked as MCAP2. When the amount of P25 was changed to 0, 0.0263, 0.0526, and 0.1052 g, the obtained samples were marked as MCA, MCAP5, MCAP10, and MCAP20, respectively.

2.3 Photocatalytic degradation of AO7

Firstly, a 20.0 mg per L AO7 aqueous solution was prepared and set in the dark for 12 h; then, 0.1 g of the obtained samples was added into 50.0 mL of AO7 aqueous solution under stirring for 1 h to achieve adsorption–desorption equilibrium. The degradation experiments were performed using a mercury lamp (250 W, UV cutoff filter with $\lambda \geq 420$ nm) with the light intensity of 2.7 mW cm^{-2}. A UV-vis spectrometer was used to analyze the solution concentration at the absorbance of 484 nm wavelength for AO7.

2.4 Photoelectrochemistry measurement

A standard three-electrode cell system was used for the photoelectrochemistry experiments, which were performed on a CHI760D electrochemical workstation (CH Instrument company, Shanghai, China). Generally, a Pt sheet electrode and a saturated calomel electrode were selected as the counter and reference electrodes. The samples coated on a nickel collector were used as the working electrodes, which were prepared as follows: 80% of MCAP, 10% of acetylene black, and 10% of poly(vinylidene fluoride) were mixed and deposited on a nickel sheet with a size of 2.0 cm × 2.0 cm. Then, the nickel sheet was set in a vacuum drying oven at 80 °C for 24 h. A 0.02 mol per L KOH solution was chosen as the electrolyte, and the samples were irradiated using a UV-light source with a cutoff filter (visible light with an irradiance of 250 W m^{-2}).

2.5 Characterization

A scanning electron microscope (SEM, Zeiss Sigma 500) was used to characterize the morphologies of the MCAPs. A Fourier transform infrared (FTIR) spectrometer (Nicolet Protege-460) was used to characterize the chemical bonds of the samples in the range of 400–4000 cm^{-1}. A UV-vis spectrometer (PerkinElmer Lambda-35) was selected to measure the UV-vis spectra of the samples. The crystal structures of the samples were measured by X-ray diffraction (XRD, Bruker D8 Advance, Germany) with Cu Kα radiation (λ = 0.154178 nm). An X-ray photoelectron spectrometer (PerkinElmer PHI-5300 ESCA) was used to collect the X-ray photoelectron spectra of the MCAPs. Nitrogen adsorption–desorption experiments were performed to characterize the pore properties of the MCAPs using ASAP 2460 apparatus from Micromeritics. Electrochemical impedance spectra (EIS) were measured by a CHI760D electrochemical workstation (CH Instrument company, Shanghai, China), and the used standard three-electrode cell system was the same as that in the photoelectrochemistry measurements. A Cary Eclipse Fluorescence Spectrophotometer (Agilent Technologies) was used to measure the photoluminescence (PL) spectra. A Vario EL III organic elemental analyzer (Various MACRO cube) and an Inductively Coupled Plasma Mass Spectrometer (EXPEC-7000) were selected to measure the element contents.

3. Results and discussion

3.1 Characterization of the MCAPs

During the synthesis of the MCAPs, the beaker was kept in a fridge. During the freezing process, as the temperature drops, H_2O molecules in the solution will gradually form solid ice crystals, while the MC dispersed in the water is gradually rejected by the ice crystals, forming a solid phase skeleton composed of MC. This solid-phase skeleton has a porous structure, and the pore size and porosity can be controlled by altering the concentration of MC in the solution and the freezing rate of the solution. Next, the water was detached from the solid phase by a thawing process. Since the solubility of MC varies with temperature, the MC will gradually migrate from the solid phase skeleton to the H_2O to form a uniform solution. The preparation of the MCAPs was a typical sol–gel process, and after the gel was dried by supercritical CO_2, the MCAP was made in the form of an aerogel. Fig. 1a shows a photo picture of MCAP20, which is a flexible membrane. As a membrane material, the photocatalyst is easily recycled. The SEM image (Fig. 1b)

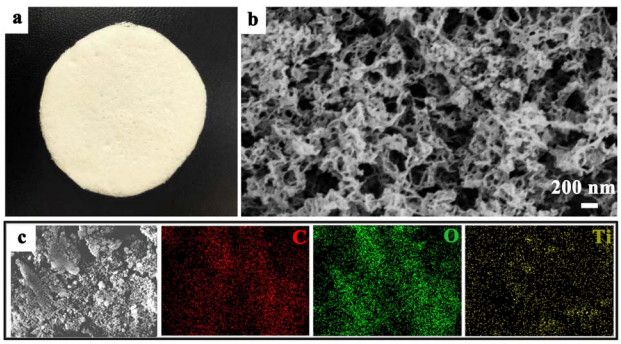

Fig. 1 Photo picture (a), SEM image (b), and mapping images (c) of MCAP20.

of MCAP20 shows that the sample consisted of tangled fibers with a diameter of *ca.* 30 nm. To analyze the element distribution, SEM mapping images were obtained. As shown in Fig. 1c, the C, O and Ti elements were uniformly distributed in the sample, indicating that the coupling of MCA and P25 was achieved.

Fig. S1† shows the XRD patterns of MCA, MCAP2, MCAP5, MCAP10, MCAP20 and P25. As can be seen, MCA shows a broad diffraction peak located from 10° to 25°, representing the amorphous scaffold of MCA. The peaks located at 14.88°, 16.08°, 22.04° and 26.01° can be ascribed to the characteristic peaks of MCA.[26] P25 is composed of 80% anatase TiO_2 and 20% rutile TiO_2. According to JCPDS card no. 21-1272, the diffraction peaks located at 25.28°, 37.76°, 48.10°, 53.90° and 62.66° correspond to the (1 0 1), (0 0 4), (2 0 0), (1 0 5), and (2 0 4) planes of anatase TiO_2; and the peaks centred at 36.08° and 41.14° are ascribed to the (1 0 1) and (1 1 1) planes of rutile TiO_2 (JCPDS no. 21-1275).[27] For the MCAPs, the XRD patterns all show the characteristic peaks of P25 and MCA. Notably, the characteristic peaks of P25 have red shifts with the P25 content increased in the MCAPs, suggesting that there are interactions between MCA and P25.

Fourier transform infrared (FT-IR) spectra were used to characterize the functional groups of the samples. As shown in Fig. 2, for MCA, the peaks located at 3395.07 and 2903.79 eV can be ascribed to the stretching vibrations of –OH groups and C–H bonds in $–CH_2$, respectively.[28] The bands located at 1667.16, 1621.84 and 1365.84 eV are attributed to the asymmetrical stretching of COO–, the symmetrical stretching of COO–, and C–H bending, respectively.[26] These peaks are all typical characteristics of a cellulosic skeleton. It can be seen that the cellulosic skeleton's intensity of MCA is decreased with the increase of the P25 content. As shown in Fig. 2, the band intensity of these areas for MCAP20 is the weakest of all the MCAPs. The decreased intensity of the –OH groups for MCA may be caused by the formation of H-bonds between MCA and P25, and thus the intensity of the –OH groups is decreased with the increase in the content of P25. Notably, the band intensity of MCAP20 at 400–800 cm^{-1} is not the weakest; this is caused by the increased content of P25, which has Ti–O and Ti–O–Ti peaks at 400–800 cm^{-1}.[27] These results reflect that the addition of P25 influences the functional groups of the MCAPs.

UV-vis diffuse reflectance spectroscopy (DRS) was used to measure the optical properties of the aerogels. As shown in Fig. 3a, the plot of P25 reflects its typical adsorption characteristics, with the adsorption area in the UV range. For the MCAPs, the adsorption intensities have an enhanced trend in the range of 400–600 nm, indicating that the coupling of P25 and MCA can improve the UV-vis light adsorption ability. The main case may be that, for one thing, the electric charge of P25 may be changed because of the coupling of MCA, and the charge transfer can be enhanced due to the presence of H-bonds.[29] For another, as aerogel photocatalysts, MCAPs are mesoporous materials, and the mesopores can reduce the light reflection and prolong the light propagation time, inducing increased photon lifetime and improved light absorption efficiency.[30,31] The Kubelka–Munk equation was used to calculate the band gaps. As shown in Fig. 3b, the band gaps of P25, MCAP2, MCAP5, MCAP10 and MCAP20 are 3.01, 2.88, 2.81, 2.60, and 2.56 eV, respectively. The valence band edges of P25, MCAP2, MCAP5, MCAP10 and MCAP20 were measured by an X-ray photoelectron spectrometer, and are 2.25, 1.80, 0.85, 0.83, and

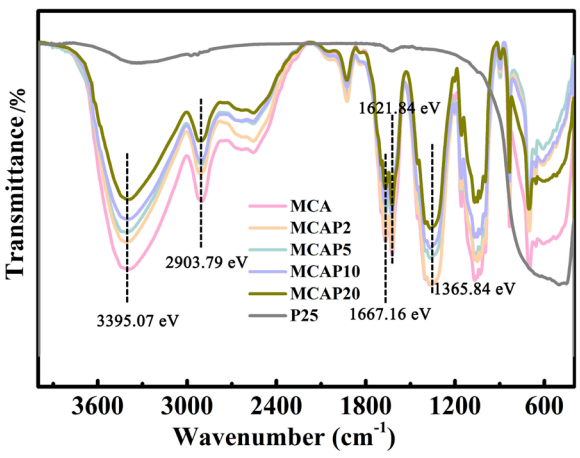

Fig. 2 FT-IR spectra of MCA, MCAP2, MCAP5, MCAP10, MCAP20 and P25.

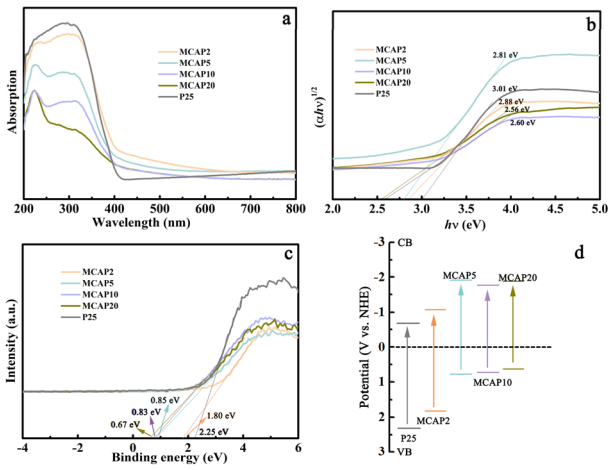

Fig. 3 UV-vis diffuse reflectance spectra (a), Kubelka–Munk plots (b), vbXPS spectra (c) and schematic band structures (d) of the samples.

0.67 eV, respectively (Fig. 3c). The corresponding schematic band structures of the samples are shown in Fig. 3d. The obtained band structures reflect that the band gaps of the MCAPs can be tuned by changing the ratio of MCA to P25. As can be seen, the MCAPs exhibit narrowed band gaps, and MCAP20 shows the narrowest band gap. In particular, the CB edges of the MCAPs are all lower than that of P25, inducing a good visible light response and enhanced reduction ability of electrons.

XPS spectra were measured to characterize the chemical states of the samples. As shown in Fig. 4a, all of the MCAPs show the characteristics of MCA, and the peaks of C 1s and O 1s are evident. Notably, as the content of P25 increases, the MCAPs show the peaks of Ti 2p. This also certified the successfully coupling of MCA and P25. Taking MCAP20 as an example, the Ti-species of P25 and MCAP20 are shown in Fig. 4b. The peaks located at 458.75 and 464.38 eV are ascribed to the Ti $2p_{1/2}$ and Ti $2p_{3/2}$ of P25, respectively,[32] and the peaks both shift in the lower binding energy direction by 0.63 eV. This may be caused by the addition of MCA, which affects the charge density of the Ti atoms.[33] The O 1s spectra of MCA, MCAP20, and P25 are shown in Fig. 4c and d. As can be seen, the O 1s peaks of MCAP20 can be divided into four peaks centred at 533.23, 532.56, 531.34, and 529.43 eV, which can be ascribed to the C–O–C, adsorbed H_2O, C–OH or adsorbed OH on Ti atoms, and defects or oxygen vacancies, respectively.[28,32] When compared with P25 and MCA, the O 1s peaks of MCAP20 exhibit a blue shift compared to those of P25, while the peaks of MCAP20 exhibit a red shift compared to those of MCA. This further implied the presence of H-bonds between P25 and MCA. Many works have certified that H-bonds promote charge transfer and reduce the recombination rate of photo-induced carriers.[34,35] Consequently, the interaction between P25 and MCA makes the MCAPs promising photocatalysts.

As a powder material, the specific surface area of P25 measured by the Brunauer–Emmett–Teller method is 14.08 cm^3 g^{-1} (Fig. 5a). In contrast, for MCA and MCAP20, the nitrogen adsorption–desorption isotherms are type IV isotherms. The specific surface areas of MCA and MCAP20 are 38.30 and 39.65 cm^3 g^{-1}, respectively. The smaller specific surface area of P25

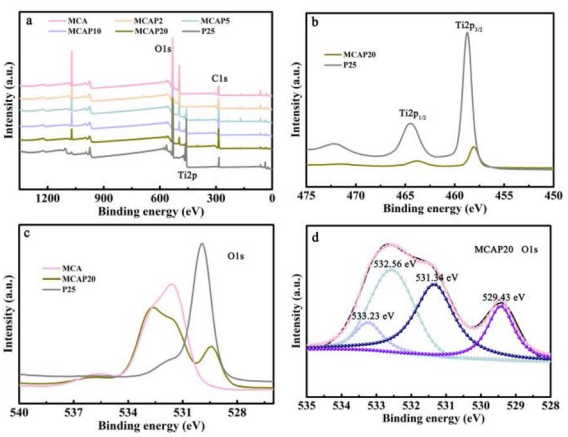

Fig. 4 XPS spectra of the samples (a), Ti 2p spectra of MCAP20 and P25 (b), and O 1s spectra of MCA, MCAP20, and P25 (c and d).

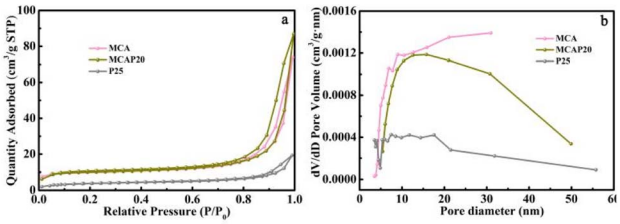

Fig. 5 Nitrogen adsorption–desorption isotherms (a) and pore size distribution plots (b) of MCA, MCAP20 and P25.

might be one factor that induces its poor photocatalytic performance. The pore size distribution plots of MCA, MCAP20 and P25 are shown in Fig. 5b. As can be seen, the plots of MCA and MCAP20 exhibit lots of mesopores, and these results are consistent with the morphologies shown in Fig. 1b. These result certify that the coupling of P25 and MCA can utilize the 3D structure of MCA, meaning that MCAP20 maintains a high surface area, which is in favor of providing more active sites for photocatalysis.[36] Furthermore, the 3D structure of MCAP makes it easy to be recycled in applications.[37]

3.2 Photocatalytic performance

Before the degradation experiments, 0.1 g of the obtained samples was added into 50.0 mL of AO7 aqueous solution under stirring for 1 h to achieve adsorption–desorption equilibrium. A UV-vis spectrometer was used to analyze the solution concentration at the absorbance of 484 nm wavelength for AO7. As shown in Fig. S2,† the AO7 removal rate increased at first, and the adsorption–desorption equilibrium was established at 20 min. For MCA, the removal rate is 52%, and the removal rates of the MCAPs are all near 42%, and are all higher than that of P25 with a removal rate of 10%. This may be caused by the chemical state of MCA and the porous structure of the MCAPs, which may provide more active sites for the adsorption of AO7.

We evaluated the photocatalytic activity of the obtained samples by the degradation of AO7. Before opening to light, the reaction was stirred in the dark for 1 h to reach equilibrium. After that, the reaction was performed under visible light (≥420 nm) irradiation. As can be seen from Fig. 6a, MCA has little degradation activity for AO7. Meanwhile, for the composite aerogels, the degradation activities of the MCAPs exhibit an upward trend with the increase of the P25 content, and they are all higher than that of pure P25. This reflects the synergistic effect of MCA and P25. The degradation rate plots were fitted according to the first-order kinetic model (Fig. 6b), which exhibits a good linearity. The rate constants (K) of MCAP2, MCAP5, MCAP10 and MCAP20 are 0.00369, 0.00757, 0.01213 and 0.01746 min^{-1}, respectively. Specifically, the K of MCAP20 is 6.6 and 436.5 times as much as that of P25 (0.00262 min^{-1}) and MCA (0.00004 min^{-1}). It may be that the MCAPs provide a high specific area for the distribution of P25, which can exhibit more active sites. More importantly, P25 and MCA are coupled by H-bonds, which play crucial roles in photocatalytic systems.[28] The charge transfer effect is critical for the photocatalytic performance of the catalysts. The charge transfer

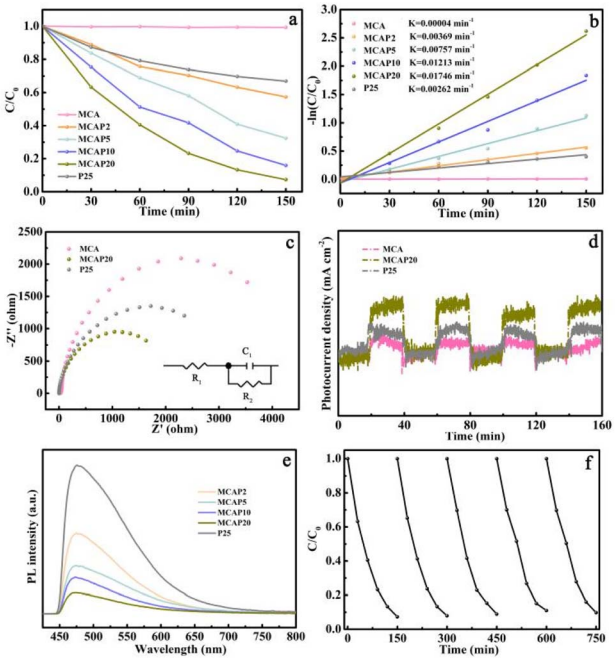

Fig. 6 Photocatalytic degradation curves of AO7 (a), the first order kinetic constants of AO7 degradation over the samples (b), EIS spectra (c), photocurrent–time curves (d), and photoluminescence spectra (e) of AO7 degradation over MCA, MCAP20 and P25, and cycling runs for AO7 degradation over MCAP20 (f).

resistances of MCA, MCAP20 and P25 were analyzed using the electrochemical impedance spectra (EIS) (Fig. 6c). Evidently, the circular diameter of the EIS Nyquist plot for MCAP20 is significantly smaller than that for MCA and P25, which indicates that MCAP20 has a smaller photoelectrode charge transfer resistance. Thus, it can be inferred that the coupling of MCA and P25 effectively reduces the photogenerated carrier transfer barrier, which can accelerate the photogenerated carrier transfer and improve the photocatalytic performance. As a commonly used organic photocatalyst, g-C_3N_4 was selected and prepared by heating dicyandiamide at 550 °C for 3 h according to the literature.[38] Besides, Ag_3PO_4/POM/GO and AgSCN/AgCl/FeOCl, which were successfully synthesized in our previous work and also showed excellent photocatalytic performance, were also selected as photocatalysts to degrade AO7.[39,40] As shown in Fig. S3,† the percentages of degradation for AO7 reached 93%, 33%, 41%, 77% and 88% over MCAP20, P25, g-C_3N_4, Ag_3PO_4/POM/GO and AgSCN/AgCl/FeOCl, respectively. The highest degradation percentage of AO7 over the MCAP certified the superiority of the MCAPs.

The photocurrent time curves were measured under visible light irradiation with a 20 s interval over MCA, MCAP20 and P25. As shown in Fig. 6d, the photocurrent density of MCAP20 is higher than that of MCA and P25. Thus, it can be inferred that MCAP20 has an enhanced photogenerated carrier separation efficiency. The same result is also reflected in the photoluminescence (PL) spectra. As shown in Fig. 6e, MCAP20 shows the weakest PL intensity, indicating that the recombination of photogenerated carriers in MCAP20 is the weakest. The PL intensity of MCAP is decreased with the content of P25. Thus, it can be inferred that the coupling of MCA and P25 can promote the separation of photogenerated carriers. Notably, the peak signals of MCAP exhibit blue shifts with the increase of the P25 content. It can be inferred that the π-conjugation systems of MCAP are extended because of the H-bonds, which can accelerate the charge transfer.[41,42] Consequently, the H-bonds play a key role in limiting the recombination of photogenerated carriers. The critical role of hydrogen bonding in the photocatalytic process was first reported by Yang *et al.*[43] They designed a surface H-bonding network-decorated g-C_3N_4 photocatalyst, and they certified by theoretical modeling that the H-bonding present can be used as a bridge, which can shorten the distance between the photocatalysts and target pollutants, and provide multiple channels for the transition of photo-carriers.

For a photocatalyst, the photocatalytic stability of the samples is the key for actual applications. In this work, the AO7 degradation activity over MCAP20 was measured five times. As shown in Fig. 6f, 92.7% of AO7 was degraded by MCAP20 in 150 min in the first cycle. Additionally, 90.3% of AO7 was degraded in the fifth cycle. Furthermore, the element contents before and after the cycling runs were measured by an elemental analyzer and inductively coupled plasma mass spectrometer. As shown in Table S1,† the content of C, O and Ti elements in MCAP20 after the fifth cycling experiment changed little compared with that before the cycling experiments, indicating that there is little loss of P25 in the process. As a result, the 3-D framework of MCA plays a key role in the fixing of P25. For one thing, this structure can inhibit the loss of P25.[44] For another, it can reduce the aggregation of P25 in the photocatalysis process. Furthermore, the sample still maintains the original morphology after the cycling experiments (Fig. S4†), which may come from the high mechanical strength of the MCA. These results all certified the photocatalytic stability of MCAP20. The good stability makes MCAP20 a promising photocatalyst in actual applications.

3.3 Photocatalytic mechanism

Based on the results above, a mechanism for AO7 degradation is determined. The enhanced photocatalytic performance is

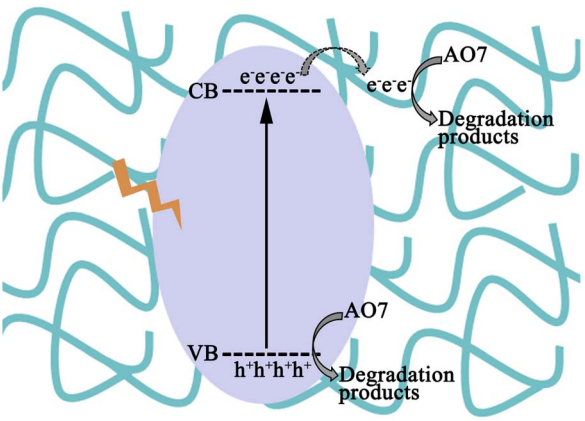

Fig. 7 A brief diagram of the AO7 photocatalytic mechanism over MCAP.

ascribed to the synergistic effect between P25 and MCA. P25 is the photoactive centre, and MCA works as an adsorbent. Furthermore, the H-bonds between P25 and MCA act as electron trappers, which can accelerate the charge transfer. Generally, as shown in Fig. 7, under the irradiation of visible light, P25 is excited and the photogenerated electrons are promoted from the VB edges to the CB edges of P25.[45,46] Then, the photo-generated electrons will be captured by MCA through H-bonds, which will limit the recombination of photo-generated carriers. Lastly, the O_2 adsorbed on the surface of MCAP will be reduced to some reactive species, such as $^1O_2$ or $^{\cdot}O_2^-$,[47,48] to attack AO7 molecules. Simultaneously, the left holes in the VB of P25 can also degrade AO7 directly. Thus, the improved charge transfer rate over MCAP20 can enhance the photocatalytic activity.

4. Conclusions

In summary, a series of MCAP photocatalysts were prepared by the sol–gel method coupling with CO_2 supercritical drying technology. The optimized MCAP20 exhibits enhanced photocatalytic performance with a AO7 degradation rate of 0.01746 min^{-1}, which is 6.6 times higher than that of P25. The good performance of MCAP20 is primarily ascribed to the H-bonds between P25 and MCA. The presence of H-bonds can efficiently transfer the photo-induced electrons and limit the recombination of photogenerated carriers. A brief diagram of the AO7 photocatalytic mechanism over MCAP is provided based on the experimental results. MCA is a hydroxyl-rich material with a 3D structure, and the coupling of MCA and P25 can not only improve the photocatalytic performance, but also solve the problem of recycling. This work certifies that the construction of H-bonds will be a good method for reforming catalysts.

Data availability

All the authors confirm that the data supporting the findings of this study are available within the article and ESI.†

Author contributions

Junhao Zeng: formal analysis, investigation, writing – original draft. Di Zhang: supervision. Guoliang Dou: formal analysis, methodology, writing – review & editing. Qingming Zeng: investigation, methodology, writing – review & editing. Jian Zhang: formal analysis and validation, writing – review & editing, funding acquisition.

Conflicts of interest

The authors declare that they have no known competing financial interests or personal relationships that could have appeared to influence the work reported in this paper.

Acknowledgements

This work was financially supported by the Science and Technology Development Plan Projects of Weifang (2022ZJ1189), Projects of 1st batch of Technology Innovation Program of Shandong Province in 2023 (202350700179), Innovation Capacity Improvement Project of Small and Medium-Sized Technology-Based Enterprise of Shandong Province (2023TSGC0706, 2023TSG C0309), and Taishan Industrial Experts Program (tscy20231238).

Notes and references

1 H. He, Z. Luo and C. Yu, Embellish zinc tungstate nanorods with silver chloride nanoparticles for enhanced photocatalytic, antibacterial and antifouling performance, *Colloids Surf., A*, 2021, **613**, 126099.
2 C. Yu, H. He, X. Liu, J. Zeng and Z. Liu, Novel SiO_2 nanoparticle-decorated BiOCl nanosheets exhibiting high photocatalytic performances for the removal of organic pollutants, *Chin. J. Catal.*, 2019, **40**, 1212–1221.
3 V. U. Pandit, S. S. Arbuj, S. S. Pandit and H. K. Gaikwad, Photocatalytic hydrogen production reactor system, *MRS Commun.*, 2022, **12**, 1190–1196.
4 V. Jawale, G. Gugale, M. Chaskar, S. Pandit, R. Pawar, S. Suryawanshi, V. Pandit, G. Umarji and S. Arbuj, Two-and three-dimensional zinc oxide nanostructures and its photocatalytic dye degradation performance study, *J. Mater. Res.*, 2021, **36**, 1573–1583.
5 S. Wang, M. Xu, T. Peng, C. Zhang, T. Li, I. Hussain, J. Wang and B. Tan, Porous hypercrosslinke polymer-TiO_2-graphene composite photocatalysts for visible-light-driven CO_2 conversion, *Nat. Commun.*, 2019, **10**, 676.
6 E. Wang, A. Mahmood, S. Chen, W. Sun, T. Muhmood, X. Yang and Z. Chen, Solar-driven photocatalytic reforming of lignocellulose into H_2 and value-added biochemicals, *ACS Catal.*, 2022, **12**, 11206–11215.
7 A. Belhameid, A. Inmaculada, O. Lorente, A. Megriche, R. Lucena and S. Ćardenas, Photocatalytic/sorption-self-cleaning activity of cellulose decorated with TiO_2 and M@TiO_2 (M=Au, Ag) polymeric nanocomposites, *J. Cleaner Prod.*, 2024, **452**, 142190.
8 Q. Cheng, Y. Yuan, R. Tang, Q. Liu, L. Bao, P. Wang, J. Zhong, Z. Zhao, Z. Yu and Z. Zou, Rapid hydroxyl radical generation on (001)-facet-exposed ultrathin anatase TiO_2 nanosheets for enhanced photocatalytic lignocellulose-to-H_2 conversion, *ACS Catal.*, 2022, **12**, 2118–2125.
9 Z. Gonzalez, J. Yus, Y. Bravo, A. J. Sanchez-Herencia, A. Rodríguez, J. Dewalque, L. Manceriu, C. Henrist and B. Ferrari, Heteroacoagulation of lignocellulose fibers-fased fiotemplates and functionalized TiO_2 nanoparticles to tailor film microstructures, *Cellulose*, 2020, **27**, 7543–7559.
10 I. Bascón-Villegas, E. Espinosa, R. Sánchez, Q. Tarrés, F. PérezRodríguez and A. Rodríguez, Horticultural plant residues as new source for lignocellulose nanofibers isolation: application on the recycling paperboard process, *Molecules*, 2020, **25**, 3275.

11 X. Zhang, S. Jing, Z. Chen, L. Zhong, Q. Liu, X. Peng and R. Sun, Fabricating 3D hierarchical porous TiO_2 and SiO_2 with high specific surface area by using nanofibril-interconnected cellulose aerogel as a new biotemplate, *Ind. Crops Prod.*, 2017, **109**, 790–802.

12 E. Espinosa, F. Rol, J. Bras and A. Rodríguez, Use of multifactorial analysis to determine the quality of cellulose nanofibers: effect of nanofibrillation treatment and residual lignin content, *Cellulose*, 2020, **27**, 10689.

13 S. Yu, X. Zhao, J. Zhang, S. Liu, Z. Yuan, X. Liu, B. Liu and X. Yi, A novel combining strategy of cellulose aerogel and hierarchically porous metal organic frameworks (HP-MOFs) to improve the CO_2 absorption performance, *Cellulose*, 2022, **29**, 6783–6796.

14 W. Zhang, X. Wang, Y. Zhang, B. van Bochove, E. Mäkilä, J. Seppälä, W. Xu, S. Willför and C. Xu, Robust shape-retaining nanocellulose-based aerogels decorated with silver nanoparticles for fast continuous catalytic discoloration of organic dyes, *Sep. Purif. Technol.*, 2020, **242**, 116523.

15 K. Li, X. Zhang, Y. Qin and Y. Li, Construction of the cellulose nanofibers (CNFs) aerogel loading TiO_2 NPs and its application in disposal of organic pollutants, *Polym.*, 2021, **13**, 1841.

16 X. Ren, Q. Yu, J. Pan, Q. Wang, Y. Li, N. Shi and S. Deng, Effect of hydrogen bond interaction in precursor on photocatalytic oxidation of MB by C-GA/g-C_3N_4 composites, *Appl. Surf. Sci.*, 2022, **606**, 154941.

17 Z. Wang, G. Ding, J. Zhang, X. Lv, P. Wang, L. Shuai, C. Li, Y. Ni and G. Liao, Correction: Critical role of hydrogen bonding between microcrystalline cellulose and g-C_3N_4 enables highly efficient photocatalysis, *Chem. Commun.*, 2024, **60**, 204.

18 H. Zhao, X. Yu, C. Li, W. Yu, A. Wang, Z. Hu, S. Larter, Y. Li, M. Golam Kibria and J. Hu, Carbon quantum dots modified TiO_2 composites for hydrogen production and selective glucose photoreforming, *J. Energy Chem.*, 2022, **64**, 201–208.

19 H. Bai, L. Yu, J. Xu, X. Pang, Y. Bai, J. Cui and W. Fan, Controllable decoration of Ni-MOF on TiO_2: understanding the role of coordination state on photoelectrochemical performance, *Chin. J. Struct. Chem.*, 2023, **42**, 100096.

20 A. Su, Q. Lei, G. Tian, Y. Yang, S. He, L. Yan, X. Hu, T. Ji, S. Li and J. Hu, An enzyme-free glucose sensing device based on TiO_2 nanorod array photoelectric catalysis, *Chin. J. Struct. Chem.*, 2023, **42**, 100133.

21 N. Parsafard, R. Abedi and H. Moodi, Ternary tin-doped titanium dioxide/calcium oxide (Sn-TiO_2/CaO) composite as a photocatalyst for efficient removal of toxic dyes, *RSC Adv.*, 2024, **14**, 19984–19995.

22 V. U. Pandit, S. S. Arbuj, Y. B. Pandit, S. D. Naik, S. B. Rane, U. P. Mulik, S. W. Gosavi and B. B. Kale, Solar light driven dye degradation using novel organo-inorganic (6, 13-Pentacenequinone-TiO_2) nanocomposite, *RSC Adv.*, 2015, **5**, 10326–10331.

23 I. Lázár, J. Kalmár, A. Peter, A. Szilágyi, E. Gyori, T. Ditrói and I. Fábián, Photocatalytic performance of highly amorphous titania silica aerogels with mesopores: the adverse effect of the *in situ* adsorption of some organic substrates during photodegradation, *Appl. Surf. Sci.*, 2015, **356**, 521–531.

24 J. Liu, J. Liu, F. Shi, S. Hu, S. Jiang, S. Liu, D. Liu and X. Tian, F/W Co-doped TiO_2-SiO_2 composite aerogels with improved visible light-driven photocatalytic activity, *J. Solid State Chem.*, 2019, **275**, 8–15.

25 H. Xu, P. Zhu, L. Wang, Z. Jiang and S. Zhao, Structural characteristics and photocatalytic activity of ambient pressure dried SiO_2/TiO_2 aerogel composites by one-step solvent exchange/surface modification, *J. Wuhan Univ. Technol., Mater. Sci. Ed.*, 2016, **31**, 80–86.

26 M. Fathy, T. A. Moghny, M. A. Mousa, A. A.-A. El-Bellihi and A. E. Awadallah, Absorption of calcium ions on oxidized graphene sheets and study its dynamic behavior by kinetic and isothermal models, *Appl. Nanosci.*, 2016, **6**, 1105–1117.

27 H. Xie, C. Hou, H. Wang, Q. Zhang and Y. Li, S, N Co-doped graphene quantum dot/TiO_2 composites for efficient photocatalytic hydrogen generation, *Nanoscale Res. Lett.*, 2017, **12**, 400.

28 Z. Wang, G. Ding, J. Zhang, X. Lv, P. Wang, L. Shuai, C. Li, Y. Ni and G. Liao, Critical role of hydrogen bonding between microcrystalline cellulose and g-C_3N_4 enables highly efficient photocatalysis, *Chem. Commun.*, 2024, **60**, 204–207.

29 Y. Han, X. Lu, S. Tang, X. Yin, Z. Wei and T. Lu, Metal-free 2D/2D heterojunction of graphitic carbon nitride/graphdiyne for improving the hole mobility of graphitic carbon nitride, *Adv. Energy Mater.*, 2018, **8**, 1702992.

30 K. Zhu, N. R. Neale, A. Miedaner and A. J. Frank, Enhanced charge collection efficiencies and light scattering in dye-sensitized solar cells using oriented TiO_2 nanotubes arrays, *Nano Lett.*, 2007, **7**, 69–74.

31 H. Li, H. Yu, X. Quan, S. Chen and H. Zhao, Improved photocatalytic performance of heterojunction by controlling the contact facet: high electron transfer capacity between TiO_2 and the {110} facet of $BiVO_4$ caused by suitable energy band alignment, *Adv. Funct. Mater.*, 2015, **25**, 3074–3080.

32 E. Han, K. Vijayarangamuthu, J. Youn, Y. Park, S. Jung and K. Jeon, Degussa P25 TiO_2 modified with H_2O_2 under microwave treatment to enhance photocatalytic properties, *Catal. Today*, 2018, **303**, 305–312.

33 R. E. Kalan, S. Yaparatne, A. Amirbahman and C. Tripp, P25 titanium dioxide coated magnetic particles: Preparation, characterization and photocatalytic activity, *Appl. Catal., B*, 2016, **187**, 249–258.

34 Q. Wu, A. Thissen, W. Jaegermann and M. Liu, Photoelectron spectroscopy study of oxygen vacancy on vanadium oxides surface, *Appl. Surf. Sci.*, 2004, **236**, 473–478.

35 J. Jun, M. Dhayal, J. Shin, J. Kim and N. Getoff, Surface properties and photoactivity of TiO_2 treated with electron beam, *Radiat. Phys. Chem.*, 2006, **75**, 583–589.

36 X. Zhao, J. Zhang, X. Wang, J. Zhang, B. Liu and X. Yi, Polyimide aerogels crosslinked with MWCNT for enhanced visible-light photocatalytic activity, *Chem.–Asian J.*, 2019, **14**, 422–430.

37 X. Zhang, S. Jing, Z. Chen, L. Zhong, Q. Liu, X. Peng and R. Sun, Fabricating 3D hierarchical porous TiO_2 and SiO_2 with high specific surface area by using nanofibril-interconnected cellulose aerogel as a new biotemplate, *Ind. Crops Prod.*, 2017, **109**, 790–802.

38 Y. Su, P. Chen, F. Wang, Q. Zhang, T. Chen, Y. Wang, K. Yao, W. Lv and G. Liu, Decoration of TiO_2/g-C_3N_4 Z-scheme by carbon dots as a novel photocatalyst with improved visible-light photocatalytic performance for the degradation of enrofloxacin, *RSC Adv.*, 2017, **7**, 34096–34103.

39 G. Liu, X. Zhao, J. Zhang, S. Liu and J. Sha, Z-scheme Ag3PO4/POM/GO heterojunction with enhanced photocatalytic performance for degradation and water splitting, *Dalton Trans.*, 2018, **47**, 6225–6232.

40 J. Song, M. Zhang, C. Yan, X. Zhao, G. Liu and J. Zhang, AgSCN/AgCl/FeOCl nanosheets heterojunction with novel interface structure and excellent photocatalytic performance, *J. Alloys Compd.*, 2020, **836**, 155544.

41 H. Li, H. Yu, X. Quan, S. Chen and H. Zhao, Improved photocatalytic performance of heterojunction by controlling the contact facet: high electron transfer capacity between TiO_2 and the {110} facet of $BiVO_4$ caused by suitable energy band alignment, *Adv. Funct. Mater.*, 2015, **25**, 3074–3080.

42 Y. G. Xu, H. Xu, L. Wang, J. Yan, H. Li, Y. Song, L. Huang and G. Cai, The CNT modified white C_3N_4 composite photocatalyst with enhanced visible-light response photoactivity, *Dalton Trans.*, 2013, **42**, 7604–7613.

43 X. L. Wang, W. Q. Fang, H. F. Wang, H. Zhang, H. Zhao, Y. Yao and H. G. Yang, Surface hydrogen bonding can enhance photocatalytic H_2 evolution efficiency, *J. Mater. Chem. A*, 2013, **1**, 14089.

44 H. Maleki and N. Hüsing, Current status, opportunities and challenges in catalytic and photocatalytic applications of aerogels: environmental protection aspects, *Appl. Catal., B*, 2018, **221**, 530–555.

45 N. Sobana, M. Muruganandam and M. Swaminathan, Characterization of ACeZnO catalyst and its photocatalytic activity on 4-acetylphenol degradation, *Catal. Commun.*, 2008, **9**, 262–268.

46 B. Krishnakumar, S. Kumar, J. Gil, V. Pandiyan, A. Aguiar and A. Sobral, Highly active P25@Pd/C nanocomposite for the degradation of Naphthol Blue black with visible light, *J. Mol. Struct.*, 2018, **1153**, 346–352.

47 X. Zhao, X. Yi, J. Song, X. Yuan, S. Yu, Y. Nie, J. Zhang and G. Cao, Mesoporous and flexible polyimide aerogel as highly active catalytic membrane for AO7 degradation by peroxymonosulfate activation, *Chem. Eng. J.*, 2022, **431**, 134286.

48 J. Yao, Y. Yu, R. Qu, J. Chen, Z. Huo, F. Zhu and Z. Wang, Fe-activated peroxymonosulfate enhances the degradation of dibutyl phthalate on ground quartz sand, *Environ. Sci. Technol.*, 2020, **54**, 9052–9061.